A theoretical study on the decomposition mechanism of artemisinin

ARTICLE *in* TETRAHEDRON · SEPTEMBER 2008

Impact Factor: 2.64 · DOI: 10.1016/j.tet.2008.07.086

3 AUTHORS, INCLUDING:

Vicent S Safont
Universitat Jaume I
84 PUBLICATIONS **1,425** CITATIONS

SEE PROFILE

Tetrahedron 64 (2008) 9448–9463

Contents lists available at ScienceDirect

Tetrahedron

journal homepage: www.elsevier.com/locate/tet

A theoretical study on the decomposition mechanism of artemisinin

Pamela Moles, Mónica Oliva, Vicent S. Safont *

Departament de Química Física i Analítica, Avda. Sos Baynat s/n, 12071 Castelló, Spain

ARTICLE INFO

Article history:
Received 3 June 2008
Received in revised form 18 July 2008
Accepted 18 July 2008
Available online 24 July 2008

Keywords:
Malaria
DFT calculations
Trioxane chemistry
C-Radical intermediates

ABSTRACT

A theoretical study on the artemisinin decomposition mechanism is reported. The suggested pathways have been reproduced and the appearance of the final products can be explained in a satisfactory way. In addition, several intermediates and radicals have been found as relatively stable species, thus giving support to the current hypothesis that some of these species can be responsible for the antimalarial action of artemisinin and its derivatives.

1. Introduction

The interest of unraveling the details of the decomposition mechanism of artemisinin (*qinghaosu*, **1**, Scheme 1) arises from the fact that artemisinins are the most potent and rapidly acting antimalarial drugs at hand nowadays.[1] Malaria remains as the foremost cause of mortality among infectious diseases currently affecting mankind.[2] The endemic malarial regions are Africa, Central and South America, and South Asia, and current projections suggest that if global warming remains unchecked, it could be re-established itself in Europe and North America.[3] Malaria causes more than 1 million deaths yearly and kills a child every 30 s.[4–7]

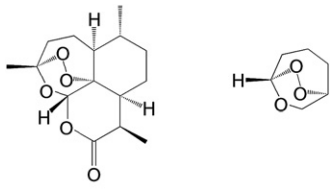

1 **1m**

Scheme 1.

There are four members of the *Plasmodium* gender that infects humans, transmitted through the bite of the Anopheles female mosquito,[8] being the *Plasmodium falciparum* the responsible for the severe malarial infections. Combinations of an artemisinin with other antimalarial drugs are now recommended treatments for *P. falciparum* malaria in most endemic areas,[9] because such combinations might be useful in delaying the emergence of artemisinin resistance.[10]

Artemisinin is a sesquiterpene lactone with an endoperoxide group and its unusual 1,2,4-trioxane ring system has been proven to be critical for the antimalarial activity.[7,11] The mechanism of action of artemisinin is not clear and is still under debate.[12,13,5,14–17] It has been suggested that different reactive intermediates are generated in the artemisinin and endoperoxide-based drugs decomposition, and that some of these could be the mediators of the antimalarial activity of this class of drugs.

The reductive cleavage of the peroxide bond in artemisinin, prompted by ferrous iron (in the form of heme or iron(II) salts), can form oxygen-centered radicals,[18] which, in turn, can lead to the formation of carbon-centered radicals.[19] These are now widely accepted (although sometimes questioned[20,1]) as key intermediates in a series of chemical reactions leading to various intermediates, one or more of which could kill the malarial parasites.[6] Definitive evidence for the generation of carbon radical intermediates during ferrous-mediated endoperoxide degradation of artemisinin and its derivatives was provided by EPR spin-trapping techniques.[21–23] Such carbon radicals have been reported as heme alkylating agents either in vitro or in vivo in infected mice,[14,24] being this alkylating activity related to the presence of the parasite in infected animals. It has also been established that artemisinin reacts much faster with heme in hemoglobin than with the free heme.[25] Alkylation of heme to form heme–artemisinin adducts has been proposed to result in the prevention of heme polymerization to non-toxic hemozoin, thus leading to the parasite death by a mechanism similar to that proposed for the chloroquine-based antimalarials.[26–29] Although

* Corresponding author. Tel.: +34 964728085; fax: +34 964728066.
E-mail address: safont@qfa.uji.es (V.S. Safont).

0040-4020/$ – see front matter © 2008 Elsevier Ltd. All rights reserved.
doi:10.1016/j.tet.2008.07.086

some studies suggested that the activity of artemisinins does not require heme,[30–33] it has been pointed out that these studies used iron chelators capable to chelate heme iron as well, and that the claims about artemisinin's effect not requiring heme can be considered as premature.[25]

Apart from heme, other molecular targets have been proposed for the reactive intermediates generated from artemisinin and its derivatives.[34–39,31] Overall, the weight of evidence and the fact that resistance has not yet developed to the artemisinins suggest that the drugs do not exert their antimalarial effects by hitting a single biological target, but rather by simultaneously hitting several targets with very high precision and efficiency.[32,5]

Several theoretical investigations have been reported on the decomposition mechanism of artemisinin and other trioxanes. The first one was made by Leszczynski et al.,[11] taking as reference framework the unified mechanism for the Fe(II) induced cleavage of artemisinin[40,22] (Scheme 2) that is nowadays generally accepted for the ferrous ion induced degradation of 1,2,4-trioxanes. Leszczynski et al. have studied the intramolecular 1,5-hydrogen shift (from **2f** to **4f**) and the homolytic C–C cleavage (from **3f** to **11f**) steps by using the molecular model 6,7,8-trioxybicyclo[3.2.2]nonane (**1m**, see Scheme 1) at the B3LYP/6-31G(d,p) level. After, Drew et al. have used artemisinin itself to study the same steps at the same theoretical level[41] and Tonmunphean et al. reported also these steps at IMOMO (B3LYP/6-31G(d,p):HF/3-21G), by using artemisinin, dihydroartemisinin, and deoxoartemisinin as molecular models,[42] as well as by using up to 12 antimalarial artemisinin derivatives.[4] In these studies, a hydrogen atom was used for modeling the single electron transfer from heme or Fe(II) in the highly acidic parasite's food vacuole, as inductor of the initial peroxide bond cleavage, so that the oxygen and carbon-centered model radicals are neutral. The acid medium in which the artemisinin decomposition process is supposed to take place favors the protonation of the putative anions as they are formed. Another calculation on these two steps, performed according to the classical bonding theory, has also recently appeared.[43]

Taranto et al.[12,44] studied the decomposition process at the semiempirical AM1 and PM3 levels by using **1** as a model, and the structures and energies of species representing **2f**, **4f**, **5**, **6**, **3f**, **11f**, **12**, **13f**, **14f** and **15** were obtained. In these papers an electron transfer is used to prompt for the peroxide cleavage, and thus the oxygen and carbon-centered model radicals are anionic. However, a more recent work by Taranto et al.[45] has appeared reporting geometries at B3LYP/6-31G(d), energies at B3LYP/6-31+G(d,p)//B3LYP/6-31G(d) levels, of models of **2f**, **4f**, **3f**, **11f**, and the two corresponding transition structures, and also some information on the energetics of **5** and **6**. In this paper, the authors use **1** as molecular model, and either an electron or a hydrogen atom to initiate the decomposition. The authors calculate neutral radicals as well as anionic radicals, and the results better agree with experiment when using the neutral ones. The solvent effects on the relative stability of some radicals derived from artemisinin have also been studied, by using the PCM/COSMO approach in water and THF solvents at B3LYP/6-31G(d) level, and it was found that the carbon radicals are more stable than the oxygen radicals.[46]

An alternative mechanistic proposal, involving the ionic scission of the peroxide bond and consequently generating a carbocation at C4, has recently been tested and discarded, so the radical pathway remains as the likeliest explanation for antimalarial activity.[2] Finally, a theoretical investigation at DFT/ZORA/TZP level, dealing with the interactions of several endoperoxides including artemisinin, with two possible sources of iron, namely the $[Fe(H_2O)_6]^{2+}$

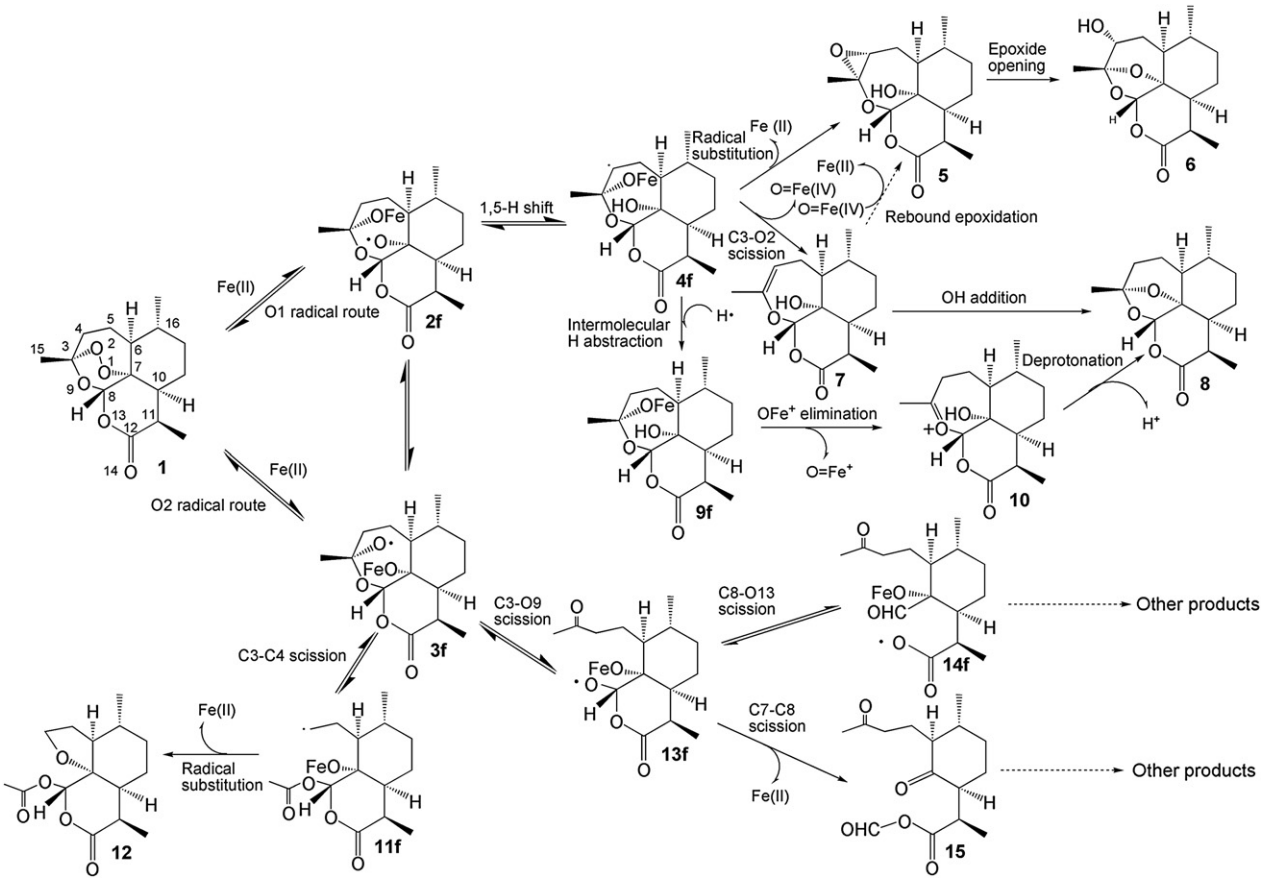

Scheme 2.

ion and heme, has been reported.[47] The authors describe an initial formation of an Fe–O bond, followed by O–O cleavage, yielding the oxygen-radical species that subsequently are transformed into the carbon-centered radicals.

Recently, we have reported a theoretical study modeling the decomposition mechanisms of artemisinin, by using 6,7,8-trioxybicyclo[3.2.2]nonane as the molecular model (**1m**, Scheme 1).[48] However, the model used did not take into account the strain and rigidity that the neighbor rings provide to the trioxane moiety. Furthermore, the model had to be somewhat enlarged, by including a six-member ring, in order to properly describe the latter steps of the O2 radical route. Thus, in the present study we have used artemisinin itself to more accurately characterize the proposed decomposition mechanisms with the aim to contribute to a better understanding of the rearrangement of endoperoxides at the molecular level.[40,22]

2. Computational methods and models

We have used a hydrogen atom to model the initial peroxide bond cleavage. As mentioned above, a single electron transfer is suggested to take place; however, due to the high acidity in parasite's food vacuole, the putative radical anions formed should be protonated as they are formed. Hence, the use of an H atom modeling the Fe(II) approaching the O–O bridge and forming an O–H bond after peroxide cleavage adequately models the situation in the human body.[42,45] All relevant stationary points shown in Scheme 3, as well as the corresponding transition structures, have been characterized at the HF/3-21G theoretical level. Then, we have further refined the calculated structures at the B3LYP/6-31G(d,p).

The stationary points have been characterized as minima or transition structures (TS) by means of a vibrational analysis. For the minima, all the wavenumbers obtained are positive, while in the case of TS, one and only one wavenumber is imaginary. This unique imaginary frequency, associated to the transition vector (TV),[49] describes the atomic motion at TS and can be used to trace the intrinsic reaction coordinate (IRC)[50] pathway that connects reactants and products. The Gaussian98[51] program package was used for the calculations.

Several species appearing along the mechanisms have an unpaired electron. For these species, the unrestricted (UHF, UB3LYP) formalisms were used and its doublet nature was confirmed by the values of the S^2 operator. Before annihilation of the first spin contaminant, the S^2 values (at B3LYP/6-31G(d,p) level) are found to range between 0.7751 and 0.7527, very close to the true doublet state S^2 value of 0.75. The spin densities for each atom were obtained by summing up the diagonal terms of the spin density matrix.

3. Results and discussion

It has been found that the decomposition of **1** renders different final products depending on the experimental conditions. For instance, if the cleavage of **1** is prompted with $FeSO_4$ in aqueous CH_3CN, the products **6** and **12** are obtained in 67% and 25% yields, respectively, while **5** is found as a minor component (1–2% yield).[22] However, if the cleavage of **1** is conducted by using $FeBr_2$ in THF/1,4-cyclohexadiene, three major products were obtained, namely **8**, **12**, and **6**, in 71%, 16.7%, and 4.2% yields, respectively.[52]

The whole experimental observations on trioxane decompositions have been satisfactorily explained by means of the

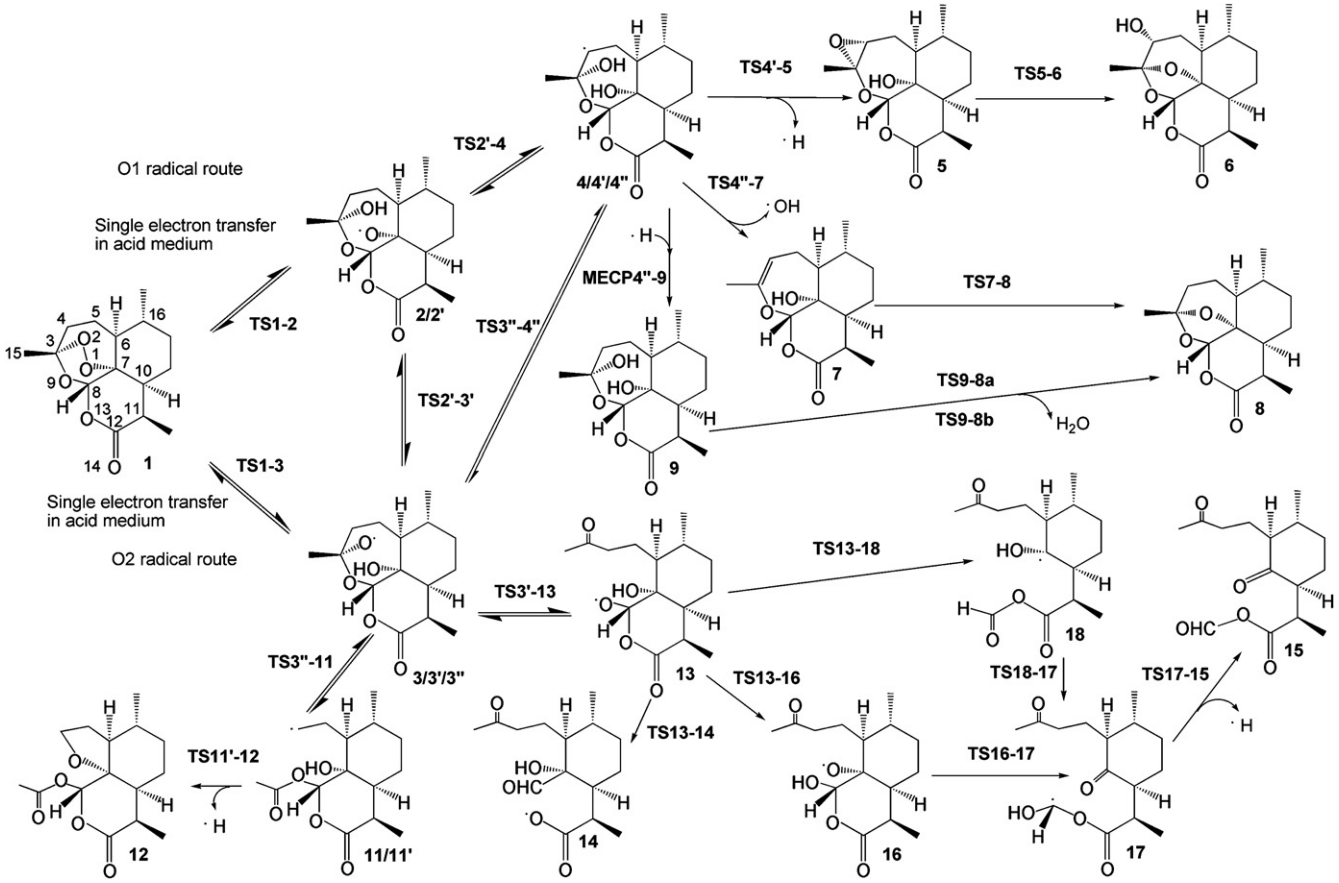

Scheme 3.

unified mechanism, shown in Scheme 2[40,22] for the artemisinin case. The process is proposed to begin with the Fe (II)-mediated cleavage of the endoperoxide bridge, yielding **2f** (O1 radical) and **3f** (O2 radical). Each one of the oxygen-centered radicals has its own routes for further evolution: O1 radical route starting from **2f** and O2 radical route starting from **3f** to give the final products. The O1 radical route can explain the appearance of the products **5**, **6**, and **8**. The O2 radical can account for the formation of **12**, among other possible decomposition products. The radicals **2f** and **3f** were postulated to be rapidly interchangeable, and we obtained a TS modeling such interconversion.[48]

In view of the complexity of the proposed decomposition mechanism, and for the sake of clarity, we are going to dissect the whole mechanism to small pieces. In this way, a detailed description of the processes can be reported step by step. Finally, to obtain a global overview of the whole mechanism, the fragments will be assembled.

3.1. The oxygen-centered radicals formation

The peroxide bond opening of **1** induced by a hydrogen atom can give either **2** or **3**, from which the O1 and O2 radical routes, respectively, can be modeled (see Scheme 3). As the H atom modeling the Fe(II) approaches O1 or O2, the O1–O2 distance in **1** smoothly increases and the energy of the system slightly rises until **TS1–2** or **TS1–3** is reached. From these TSs, following the IRC path, the local minima **2** (O1 radical) and **3** (O2 radical) are found, respectively. The O1–O2 bond has been broken and the unpaired electron is localized mainly at O1 or O2 atoms.

A link between the O1 and O2 radical routes has been found to take place by means of a hydrogen exchange between O2 and O1, via **TS2′–3′**. This TS is the theoretical evidence that the O1 and O2 radical routes are interconnected, giving support to the previous proposals about this fact and confirming the results obtained in our previous study.[48] From **TS2′–3′**, the local minima **2′** and **3′**,

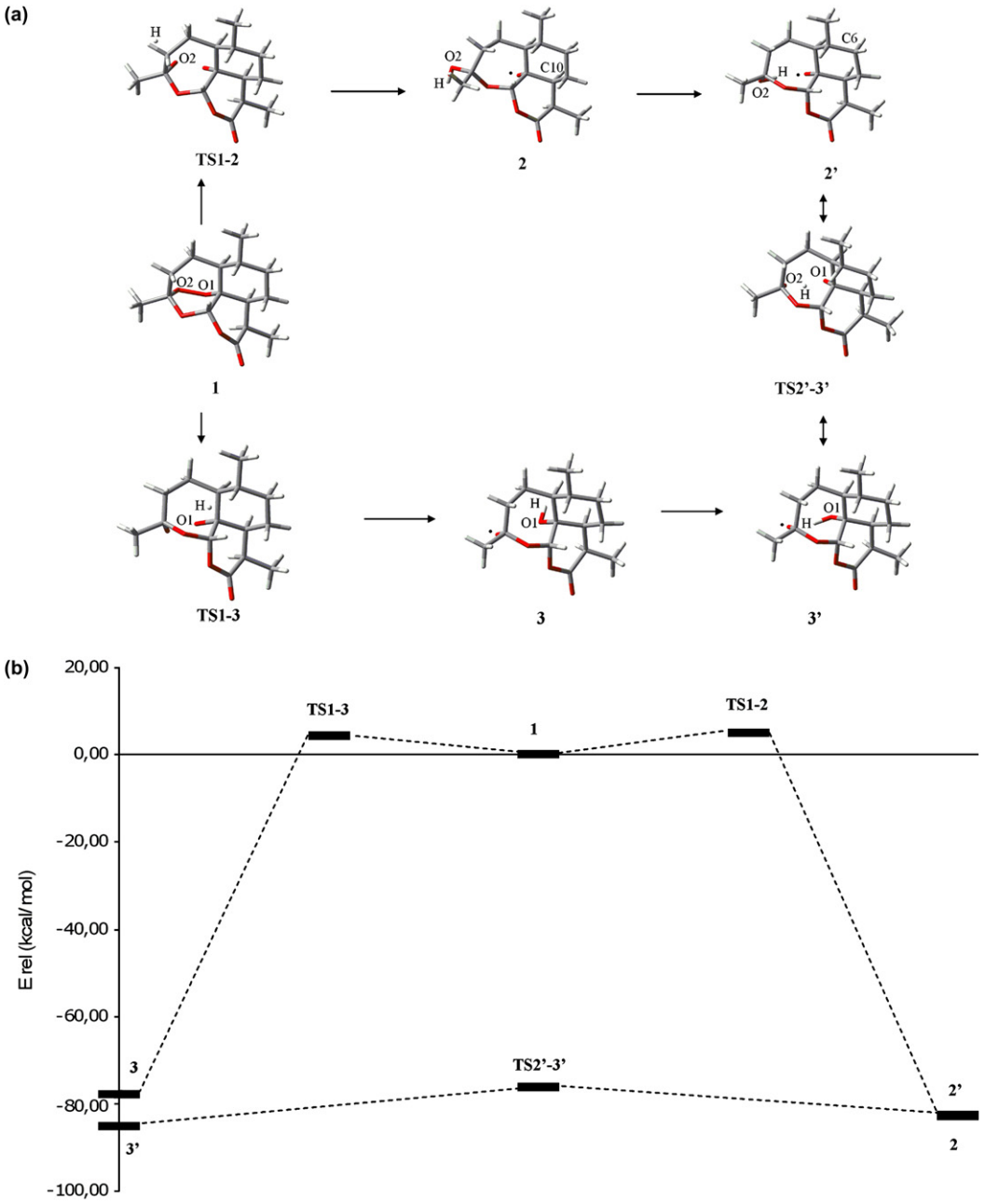

Figure 1. (a) Stationary points **1**, **2**, **2′**, **3**, **3′**, **TS1–2**, **TS2′–3′**, and **TS1–3**. (b) Energy profiles for the steps leading from **1** to the *O*-centered radicals at B3LYP level.

conformers of **2** and **3**, respectively, are found. It should be noted that we obtain the two minima associated to each TS by following the IRC path, and this gives rise in some cases to different conformations representing the same species. For the sake of completeness, we report the geometry and energy of all the conformers found. It should also be noted that in the actual system, at **TS2′–3′** the Fe(III) ion has to move from one oxygen to another, instead of an H atom. Preliminary calculations from our group, not shown here, including the ferric ion, suggest that a TS describing this interchange process do exists.

In Figure 1a, the stationary points **1**, **2**, **2′**, **3**, and **3′**, as well as **TS1–2**, **TS1–3**, and **TS2′–3′**, obtained at B3LYP/6–31G(d,p) theoretical level, are depicted. The corresponding structures obtained at HF/3-21G level are not reported and are available from the authors on request.

In Table 1, the S^2 operator values and the spin densities on selected atoms are reported for the stationary points found, as obtained by using the B3LYP calculations. The corresponding results calculated at the HF level are found to be less adequate, because some residual spin contamination is found, mainly for the TSs, and are not herein reported. The spin density at **TS1–2** and **TS1–3** is shown to concentrate on the H atom being incorporated to the model molecule, with some delocalization to the O1 and O2 atoms, respectively. At **2** and **2′**, the unpaired electron is mainly found on the O1 atom, while at **3** and **3′** (and also at **3″**, see below) it is mainly localized on the O2 atom. It is interesting to note that the conformational difference between **2** and **2′**, and between **3** and **3′** (and **3″**), produces small changes at the electronic level. Thus, some residual spin density accumulates on C10 at **2**, while at **2′** it is C6 the atom on which some spin density can be found. On the other hand, the differences in the spin distribution between **3** and **3′** (and **3″**) can mainly be sensed in the spin density value found on C4 and C15 atoms. It is also interesting to note that at **TS2′-3′** the spin density is found on both O1 and O2 atoms, and not on the H atom being transferred.

The energetic values of these structures are reported in Table 2; the corresponding values at HF/3-21G level are reported as Supplementary data. We have calculated the reference energy as the sum of the energies of **1** and the H atom that, as commented above, accounts for the single electron transfer in the acidic parasite's food vacuole. In Figure 1b, the energy profiles are drawn. It can be seen that the O2 pathway is slightly favored according to the reported results, suggesting an initial preference for such route. However, it can also be seen that the transition structure **TS2′–3′**, that connects the O1 and O2 routes, can be easily attained, and hence the two radical routes are equally opened once the process begins.

The imaginary frequencies, the negative eigenvalues, and the main components of the TVs for **TS1–2**, **TS1–3**, and **TS2′–3′** are reported as Supplementary data. Transition states **TS1–2** and **TS1–3** are associated to the O1–O2 breaking bond and the H–O2 or H–O1 forming bonds, as expected, while at **TS2′–3′** the motion of the hydrogen atom that is being exchanged between O1 and O2 dominates the fluctuation pattern.

3.2. The carbon-centered radicals formation

An intramolecular hydrogen shift from C4 to O1, via **TS2′–4**, connects the O1 radical species with the secondary carbon-centered radical **4**. On the other hand, a C3–C4 scission on the O2 radical species through the **TS3″–11** yields the C4 primary radical **11**. Following the IRC path from **TS3″–11**, we have found **3″**, a third and slightly more stable conformation for the O2 radical.

According to the results summarized in Table 1, **TS2′–4** shows a situation with the radical character partitioned between C4 and O1, and at **4** the unpaired electron is mainly localized on C4, as expected. At **TS3″–11**, a larger spin density is found on C4 than on O2 and hence this TS has a late character. Finally, at **11** the unpaired electron is found on C4.

Table 1
S^2 operator values for the stationary points indicated. Spin densities (S) on selected atoms. The B3LYP/6–31G(d,p) values are shown

S^2		S		S^2		S	
TS1–2	0.7719	H	0.80	**TS1–3**	0.7744	H	0.81
		O1	0.18			O2	0.18
2	0.7533	O1	0.86	**2′**	0.7538	O1	0.80
		C10	0.10			C6	0.13
3	0.7534	O2	0.84	**3′**	0.7540	O2	0.76
		C4	0.07			C4	0.16
		C15	0.10			C15	0.07
TS2′–3′	0.7559	O2	0.43	**TS2′–4**	0.7560	C4	0.46
		O1	0.47			O1	0.50
4	0.7540	C4	0.96	**3″**	0.7534	O2	0.84
		C5	0.07			C4	0.10
		C3	−0.06			C15	0.08
		C6	0.05				
TS3′–11	0.7643	C4	0.62	**TS3″–4″**	0.7574	C4	0.52
		O2	0.40			O2	0.54
		C3	−0.08				
4′	0.7539	C4	1.00	**4″**	0.7541	C4	0.99
		C5	−0.08			C5	−0.08
		C6	0.06			C3	−0.05
		H_{C4}	−0.05			C6	0.06
						O2	0.06
						H_{C4}	−0.05
TS4′–5	0.7666	H_{O2}	0.77	**TS4″–7**	0.7597	C4	0.29
		C4	0.36			O2	0.74
		O2	0.11				
11	0.7537	C4	1.05	**11′**	0.7536	C4	1.02
		C5	−0.08			C5	−0.07
		H_{C4}	−0.05			H_{C5}	0.06
		H_{C5}	0.06				
TS11′–12	0.7604	H	0.62	**TS3′–13**	0.7632	O2	0.44
		C4	0.39			O9	0.43
		O1	−0.06			C3	−0.10
						C7	0.05
						H_{C8}	0.06
13	0.7560	O9	0.54	**TS13–14**	0.7751	O9	0.49
		C7	0.23			O13	0.43
		O1	0.09			O14	0.23
		H_{C8}	0.09			C8	−0.14
						C12	−0.06
14	0.7560	O14	0.57	**16**	0.7539	O1	0.79
		O13	0.48			C10	0.07
		C12	−0.08			C6	0.11
TS16–17	0.7570	O1	0.54	**17**	0.7527	C8	0.84
		C8	0.25			O9	0.06
		C10	0.06			O13	0.05
		O13	0.06				
TS17–15	0.7635	H_{O9}	0.75	**TS13–18**	0.7563	O9	0.58
		C8	0.32			C7	0.24
		O9	−0.11			C8	0.09
18	0.7535	C7	0.83	**TS18–17**	0.7560	C8	0.47
		C6	−0.06			C7	0.34
		O1	0.07			O13	0.05
		H_{C6}	0.05				
		H_{C10}	0.06				

Table 2
Energy values (E, hartree/particle) for the indicated stationary points obtained at B3LYP level. Relative energies (E_{rel}, kcal/mol) to **1** plus an H atom

	E	E_{rel}
1+H	−961.408491	0.00
TS1-2	−961.400435	5.06
2	−961.540628	−82.92
2′	−961.540208	−82.65
TS1–3	−961.401837	4.18
3	−961.532598	−77.88
3′	−961.544363	−85.26
TS2′-3′	−961.530139	−76.32

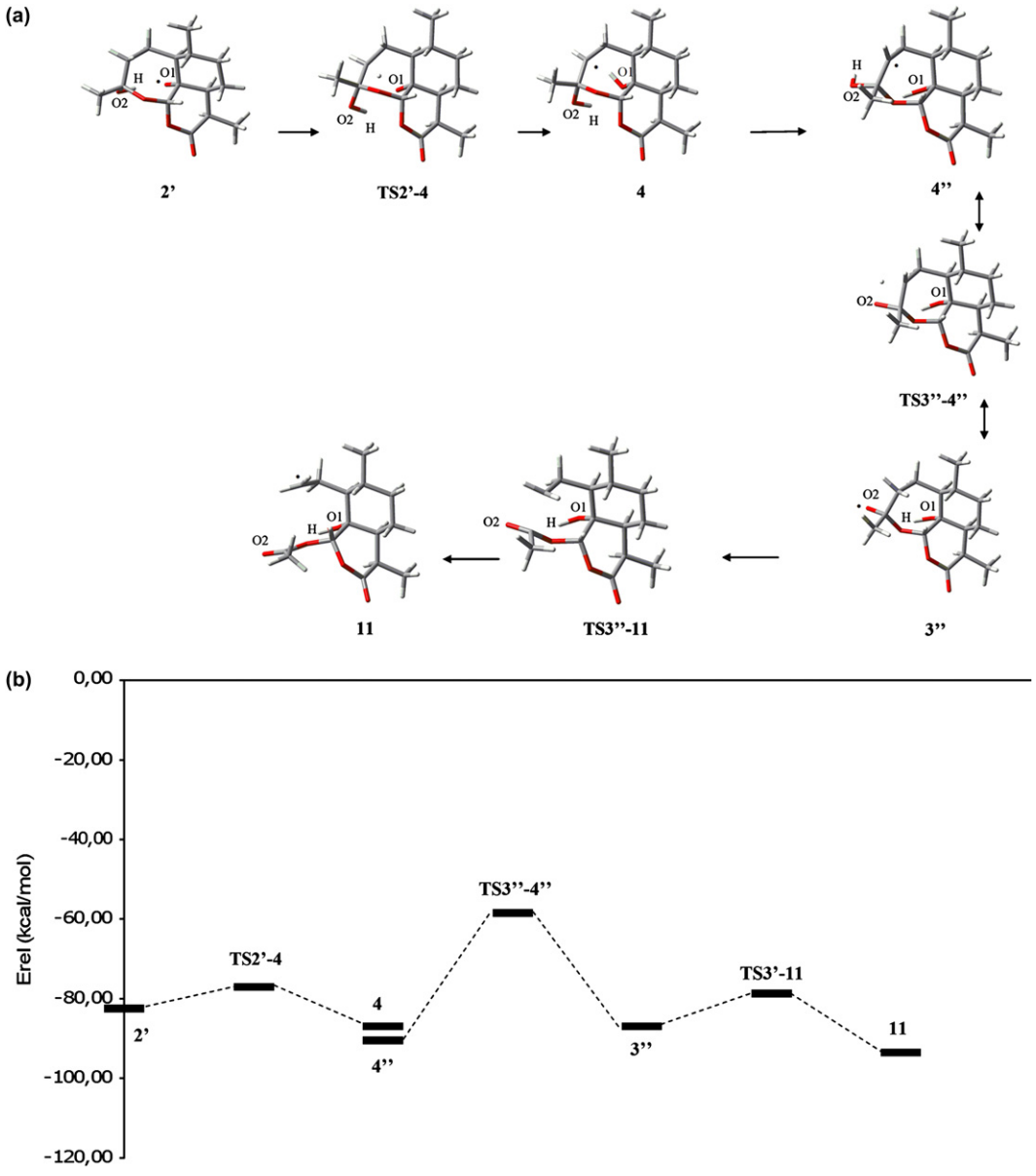

Figure 2. (a) Stationary points **2′**, **4**, **4″**, **3″**, **11**, **TS2′–4**, **TS3″–11**, and **TS3″–4″**. (b) Energy profiles for the steps leading from **2′** to **4**, from **3″** to **11**, and from **3″** to **4″** at B3LYP level.

In Figure 2a, the stationary points **2′**, **4**, **4″**, **3″**, and **11**, as well as **TS2′–4**, **TS3″–11**, and **TS3″–4″**, are depicted. The energetic values of these species are reported in Table 3 and the corresponding energy profiles are presented in Figure 2b. It can be seen that the carbon-centered radicals are more stable than the corresponding oxygen-centered radicals, as expected. The whole process from **1** to either **4** or **11** is found to be highly exothermic, thus giving support to the proposed *C*-centered radical formation. The species **11** is found to be the most stable structure within these initial steps, and hence it seems again that the O2 radical route can be thermodynamically favored, at least until the *C*-radicals are formed. Interestingly, it has been found that this species alkylate heme in infected mice and this alkylation process is possibly the only malarial-parasite relevant fully characterized alkylation reaction reported to date.[15,24]

Table 3
Energy values (*E*, hartree/particle) for the indicated stationary points obtained at B3LYP level. Relative energies (E_{rel}, kcal/mol) to **1** plus an H atom

	E	E_{rel}
2′	−961.540208	−82.65
TS2′–4	−961.531302	−77.07
4	−961.547214	−87.05
4″	−961.552871	−90.60
3″	−961.547299	−87.10
TS3″–11	−961.533968	−78.74
11	−961.557871	−93.74
TS3″–4″	−961.501805	−58.56

Within the context of our calculations, a second link between the two radical routes studied has been found, via **TS3″–4″**. In such TS, a hydrogen transfer from O2 to C4 connects the carbon-centered radical **4″** with the oxygen-centered radical **3″**. However, the significance to the actual system of this transition structure has to be put into jeopardy, because **4″** species obtained from **3″** would not model **4f** species appearing in Scheme 2: the Fe atom would remain bonded to O1 and a hydrogen atom would replace the Fe linked to O2 in **4f**. Also, **3″** species obtained from **4″** would not model **3f**, because the Fe atom would remain linked to O2 and a hydrogen atom would replace the Fe linked to O1 in **3f**. Hence, if this transition structure did exist in the actual system, new pathways rarely proposed in the literature would be opened, giving rise to products

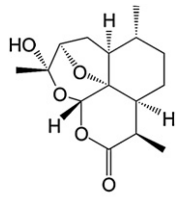

19

Scheme 4.

like **19**, see Scheme 4. In fact, the species **19** has recently been proposed to contribute to similar yields of O1 and O2 radical routes.[53] Transition state **TS3″–4″** shows its radical character partitioned between C4 and O2, and no significant spin density is found on the H atom being transferred, see Table 1.

The imaginary frequencies, the negative eigenvalues, and the main components of the TVs for **TS2′–4**, **TS3″–11** and **TS3″–4″** are reported as Supplementary data. The TSs are associated to the expected atom motions.

3.3. The obtention of 6

A two-step pathway has been proposed in the literature to obtain **6**, one of the major products experimentally obtained in the artemisinin decomposition, once the C4 secondary radical **4f** (see Scheme 2) has been reached. In the first step, the Fe(II) ion is released to obtain the epoxide species **5**, identified as a minor component in the products' mixture in some artemisinin cleavage experiments. Then, the epoxide opening concerted with the lactone ring closure and the H migration from O1 to O2 gives raise to the product **6**. We have theoretically modeled this pathway (Fig. 3a) via **TS4′–5** that leads to the epoxide intermediate **5**, and then, through **TS5–6** that describes the lactone closure and H_{O1} migration, **6** is finally obtained. It is worth noting that the H_{O2} that is eliminated in

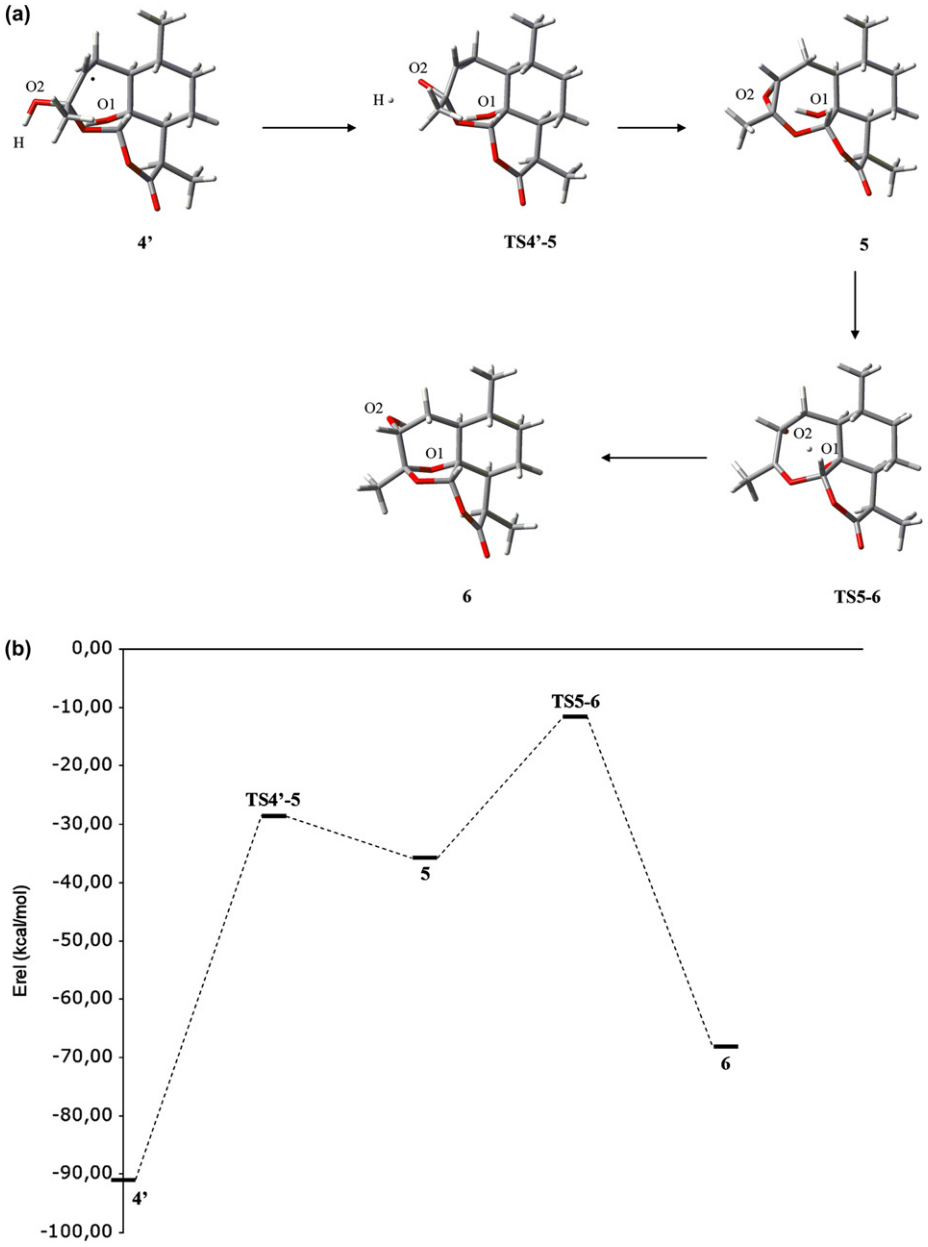

Figure 3. (a) Stationary points **4′**, **5**, **6**, **TS4′–5**, and **TS5–6**. (b) Energy profiles for the steps leading from **4′** to **6** at B3LYP level.

Table 4
Energy values (E, hartree/particle) for the indicated stationary points obtained at B3LYP level. Relative energies (E_{rel}, kcal/mol) to **1** plus an H atom

	E	E_{rel}
4′	−961.553667	−91.10
TS4′–5	−961.454216	−28.69
5+H	−961.465570	−35.82
TS5–6+H	−961.426899	−11.55
6+H	−961.517238	−68.24

the first step from the model molecule is the H atom that had entered at O2 in the first step of the global process, and hence it represents the Fe(II) ion in the actual system.

The energetics of the calculated steps are reported in Table 4 (B3LYP results) and in Supplementary data (HF results), and the obtained profiles are depicted in Figure 3b. The epoxide intermediate plus an H atom were found to be ca. 55 kcal/mol (62 kcal/mol with HF) more unstable than the secondary radical **4′**. Hence, although the energy value for the epoxide species still lies under the starting reactants (**1** plus an H atom) energy, and its formation is an exothermic process, other pathways nonrequiring the epoxide formation would be preferred within the artemisinin decomposition process.

These results suggest that the epoxide intermediate would not probably be responsible of the antimalarial activity, because the *C*-centered and even the *O*-centered radicals are found to be more stable species. This observation is in agreement with the recent work by Taranto et al.[45] and confirms our previous results.[48]

The main components of the TV associated to **TS4′–5** and **TS5–6**, as well as the imaginary frequency values and selected geometric parameters are reported as Supplementary data. The fluctuation pattern obtained describes in the first case the breaking of the O2–H_{O2} bond and the O2–C4 closure. These two motions participate antisymmetrically in the TV. On the other hand, the TV

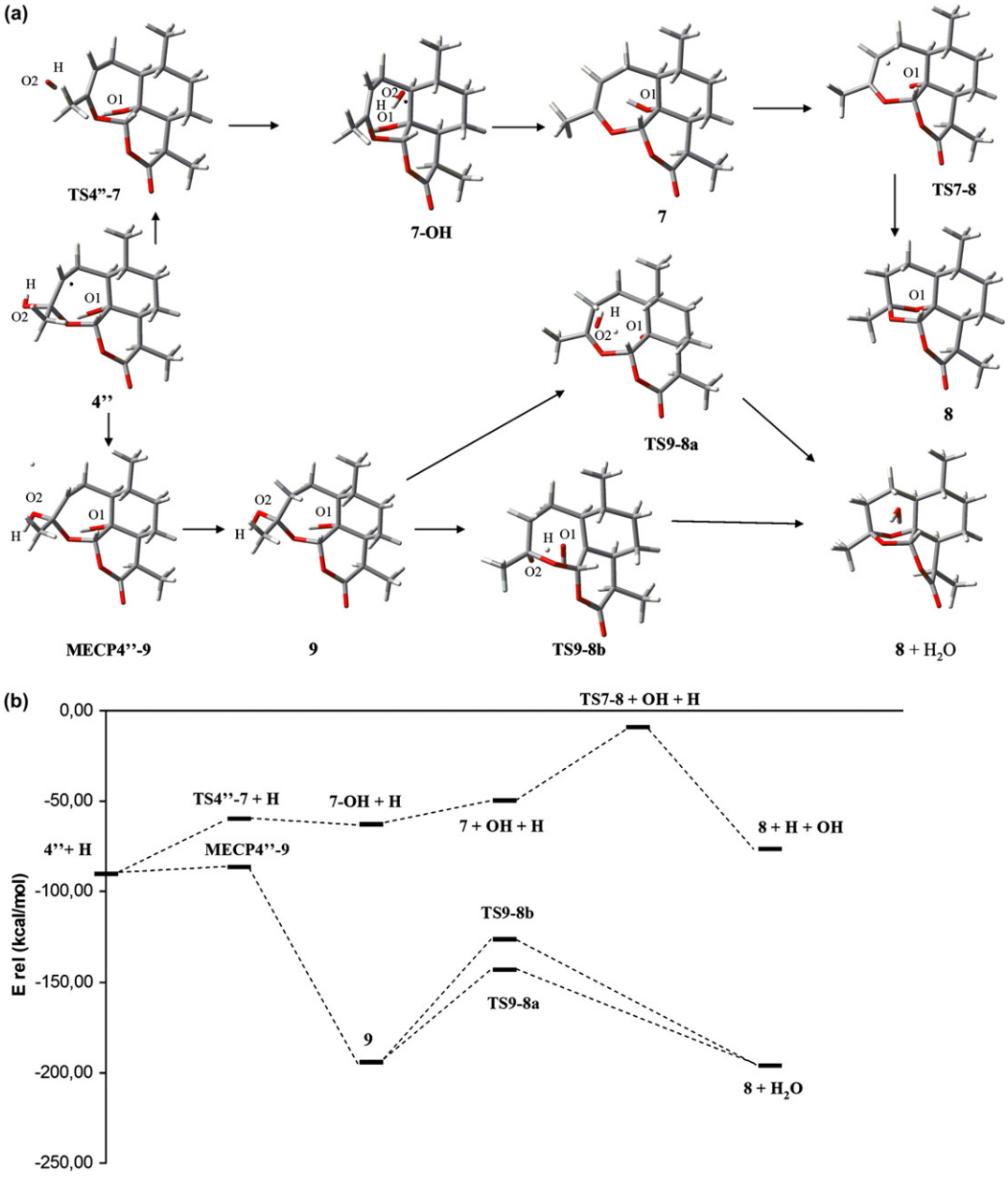

Figure 4. (a) Stationary points **4″**, **7**, **7-OH**, **8**, **9**, **TS4″–7**, **TS7–8**, **MECP4″–9**, **TS9–8a**, and **TS9–8b**. (b.) Energy profiles for the steps leading from **4″** to **8** at B3LYP level.

associated to the **TS5–6** shows a large number of components associated to the process, with the H_{O1} motion from O1 to O2 as the main one, especially at the B3LYP level, with a very important participation of the H_{C4}–C4–C3–O9 dihedral angle. Although the particular TV component values depend on the coordinates defined, it is concluded that a large portion of the molecule participates in the epoxide opening and the final ring closure to yield **6**.

The spin density at **TS4′–5** concentrates at H_{O2} and, to a lower extent, at C4 (see Table 1), with a small delocalization to O2.

3.4. The obtention of 8

As can be seen in Scheme 2, two alternative paths were proposed starting from **4f** to account for the outcome of **8**. The first one begins with the C3–O2 scission with O=Fe(IV) release to yield the alkene **7** that can be rearranged to render **8**. The second one starts with a hydrogen abstraction from the media to render **9f**, which, via the consecutive OFe^{+} elimination and deprotonation, finally gives **8**. To model the first proposed alternative, we have obtained **TS4″–7**, which accounts for an OH elimination representing the O=Fe(IV) release (see Fig. 4a). Subsequently, the alkene intermediate can be rearranged to **8** via **TS7–8**.

However, as it was the case in our previous report,[48] we were not able to obtain a TS connecting the secondary C4 radical with **9**. In the same way that we described in that paper, we have taken into account that the C4 radical plus a hydrogen atom is a system with a global triplet multiplicity, while **9** is a singlet. Thus, we have conducted a search for the Minimum Energy Crossing Point (MECP) between the triplet and singlet hypersurfaces in the vicinities of the structures of interest by means of the Harvey algorithm. Such procedure minimizes a generalized gradient obtained from the combination of the energies and gradients of the two potential energy surfaces that cross each other.[54] In such a way, we have found the MECP reported in Figure 4a. From this MECP, an optimization in triplet state (without the hydrogen atom) yields **4″**, while an optimization in the singlet state renders **9**. From this structure, via two alternative TSs describing the water elimination coupled with the ring closure (cf. **TS9–8a** and **TS9–8b**), we obtained finally **8** plus a water molecule. It is worth noting that within our model we could not substantiate the intermediation of a species modeling **10** (see Scheme 2). Instead, **9** to **8** conversion has been described as a single step with two alternatives depending on which oxygen is eliminated from the system to form the water molecule (see Scheme 3). These two alternative steps model the Fe(III)OH release to give the final product **8**.

The energetic values are reported in Table 5, and in Figure 4b, the energetic profiles obtained for these pathways are depicted. The two calculated pathways linking **4″** with **8** are not equivalent within our model, because the first pathway connects **4″** with **8** plus a hydroxyl radical, while the second one corresponds to the process from **4″** plus a hydrogen radical abstracted from the media to give **8** plus a water molecule. To make possible the comparison among the energetic values of these structures, we have added a spectator hydrogen radical to the first pathway. In such a way, the two sequences would begin at the same point and comparisons can be done. The first sequence would be as follows:

$$\mathbf{4''} + H \rightarrow \mathbf{TS4''\text{–}7} + H \rightarrow \mathbf{7} - \mathbf{OH} + H \rightarrow \mathbf{7} + OH + H \rightarrow \mathbf{TS7\text{–}8} + OH + H \rightarrow \mathbf{8} + OH + H.$$

The second sequence would be:

$$\mathbf{4''} + H \rightarrow \mathbf{MECP4''\text{–}9} \rightarrow \mathbf{9} \rightarrow \mathbf{TSs9} - \mathbf{8} \rightarrow \mathbf{8} + H_2O.$$

The relative energies have been calculated with respect to **1** plus two hydrogen atoms.

If there is a source of H in the medium the second path is found to be preferable, because the obtention of **9f** (modeled by the species **9** in our calculations) implies a new C–H bond formation that provides a huge stabilization to the system. The final passage from **9** to **8** plus a water molecule, via the two competitive TSs, is found to be slightly exothermic. On the other hand, if there is not a source of H in the medium, the first route provides a path for the outcome of **8**, one of the experimentally detected products in the artemisinin decomposition. This path implies the OH elimination from the model molecule **4″**, and our calculations predict a slight destabilization (by ca. 14 kcal/mol) of the system when going from **4″** to **8** plus the OH radical. It must be noted that we have not explored further processes in which the OH radical, representing the O=Fe(IV), released from the system could be involved. In any case, the existence of two alternative mechanisms assures that **8** will be reached, as it is observed experimentally.

The main components of the TVs are reported as Supplementary data. The **TS4″–7** describes the OH release from the molecule, coupled with the C3–C4 double bond formation. At B3LYP, a hydrogen bond complex (**7-OH**) between the leaving OH and the O1 atom was found in the path from the TS to **7**. The distance between O1 and the leaving OH is 1.86 Å. After this complex is found, the departure of the OH radical gives raise to the separate species **7** and OH, with an energy increase of 13.18 kcal/mol. The **TS7–8** shows a global fluctuation of the molecule, which is being rearranged to the bicyclic structure **8**. The fluctuations at **TS9–8a** and **TS9–8b** are not limited to a particular fragment, but almost all the atoms in the molecule participate with its motions to H_2O leaving to reach **8**.

As can be seen in Table 1, the spin density at **TS4″–7** is mainly located at O2, with some delocalization to C4.

3.5. The obtention of 12

The obtention of **12** was proposed to take place starting from the C4 primary radical **11f**, via a one-step path. The species **12** is another of the major products experimentally obtained in the artemisinin decomposition (see Scheme 2). In this step, the Fe(II) ion is released.

We have modeled this pathway (see Fig. 5a) via the **TS11′–12**. The local minimum obtained following the IRC path on the reactant side from the TS, **11′**, has a conformation slightly different from that of **11**, and is favored by ca. 5 kcal/mol. The **TS11′–12** describes the H (representing Fe(II) ion) release from O1 and the coupled closure of the furan ring. The energetic values of the calculated steps are detailed in Table 6 and depicted in Figure 5b.

The radicals **11** and **11′** present a similar spin density distribution (see Table 1), with the unpaired electron localized at C4. At **TS11′–12**, the spin density appears on H and C4, with a very minor participation of O1.

Table 5
Energy values (E, hartree/particle) for the indicated stationary points obtained at B3LYP level. Relative energies (E_{rel}, kcal/mol) to **1** plus two H atoms

	E	E_{rel}
4″+H	−962.053144	−90.60
TS4″-7+H	−962.004134	−59.85
7-OH+H	−962.009122	−62.98
7+OH+H	−961.988133	−49.80
TS7-8+OH+H	−961.923471	−9.23
8+OH+H	−962.031122	−76.78
MECP4″-9	−962.047071	−86.79
9	−962.219137	−194.76
TS9–8a	−962.137151	−143.32
TS9–8b	−962.110240	−126.43
8+H_2O	−962.222104	−196.62

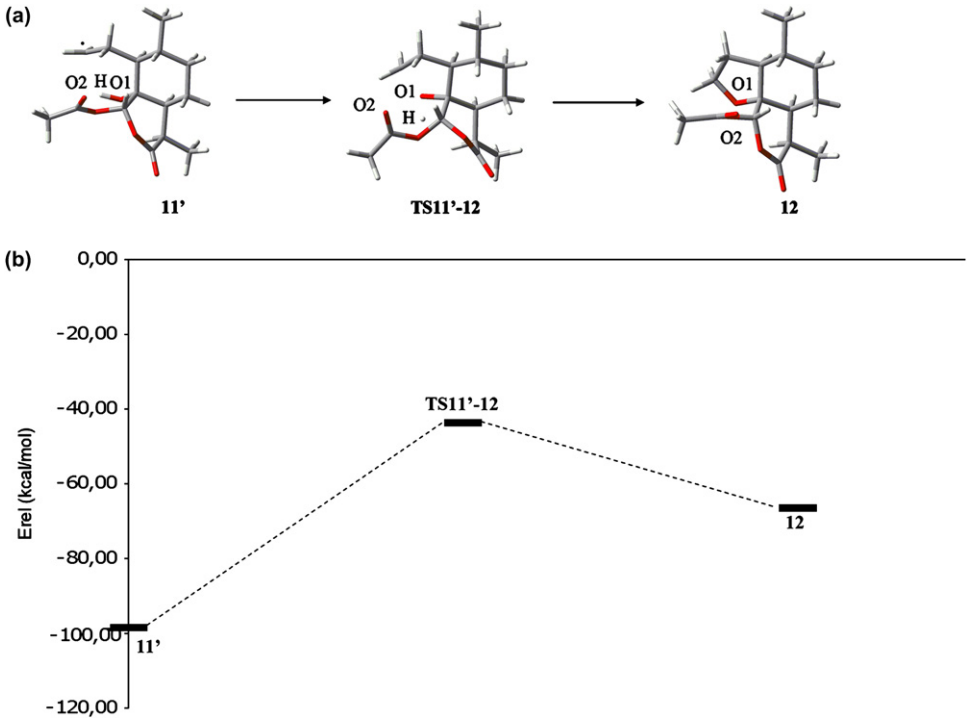

Figure 5. (a) Stationary points **11′**, **12**, and **TS11′–12**. (b) Energy profiles for the steps leading from **11′** to **12** at B3LYP level.

Table 6
Energy values (E, hartree/particle) for the indicated stationary points obtained at B3LYP level. Relative energies (E_{rel}, kcal/mol) to **1** plus an H atom

	E	E_{rel}
11′	−961.565762	−98.69
TS11′–12	−961.478144	−43.71
12+H	−961.514588	−66.58

3.6. The obtention of 14

If a C3–O9 scission takes place at the **3f** radical, the O9 radical **13f** would be obtained (see Scheme 2). Such species would be the intermediate to explain the appearance of **15** and other products derived either from **15** itself or from the oxygen-radical **14f**. Although these species are not the main products observed in the experimental artemisinin decomposition studies, they have been sometimes detected.[55]

The obtaining of **13f** from **3f** has been modeled to occur through **TS3′–13**. In Figure 6a, the structures of **3′**, **TS3′–13**, and **13** are presented. The energy values are reported in Table 7 and the energy profiles are depicted in Figure 6b. The barrier height is quite low and thus this step would be a competitive pathway inside the O2 radical route. The breaking of the O13–C8 bond at **13**, via **TS13–14**, would render the O radical **14**.

At **TS3′–13**, the spin density can be found partitioned between O2 and O9 (see Table 1), with some negative participation of C3. At **13**, the unpaired electron is located on O9 and, to a lesser extent, on C7. Thereafter, at **TS13–14**, a strong delocalization of the unpaired electron is found, and the spin density is widespread mainly on O9, O13, and O14. Finally, at **14**, the unpaired electron is delocalized between O13 and O14.

Transition state **TS3′–13** is clearly associated to the opening of the ring, see Supplementary data, with a significant participation of O2–C3 bond that evolves to a double bond in **13**, and angles and dihedrals related with the ring opening. The main component in the TV associated to **TS13–14** is the O13–C8 bond distance, because this bond is being broken, and some angles and dihedrals are found to participate also in the TV.

3.7. The obtention of 15

To obtain **15**, another pathway has been proposed starting from **13f**: a C7–C8 scission with Fe(II) release would render the final species **15** and derived products (see Scheme 2). However, we have found that this pathway is not a single step. Instead, two alternative paths have been calculated starting from **13** and ending up at **15** (see Scheme 3): the first one would start with the C7–C8 breaking (via **TS13–18**) to render the C7 radical **18**, which in turn would suffer an intramolecular hydrogen transfer between O1 and O9 through **TS18–17**, yielding the C8 radical **17**. It is worth noting that the H motion from O1 to O9 represents the Fe(III) motion in the actual system.

The second one would start with the H migration from O1 to O9 through the **TS13–16**, yielding the O1 radical **16**. Thereafter, the C7–C8 bond breaking would take place, via **TS16–17**, and in this way **17** can be obtained again. This second alternative was not completely characterized by using the B3LYP/6-31G(d,p) calculation level, because all efforts to find the **TS13–16** were unsuccessful at this level, although it was easily obtained at HF/3-21G. Instead, different conformers of **TS18–17** were found, thereby suggesting that the C7–C8 breaking precedes the hydrogen shift from O1 to O9. Transition state **TS16–17** has also been obtained by using the B3LYP approach and it is reported for the sake of completeness. Finally, once **17** has been reached, the H release from O9 via **TS17–15**, representing the Fe(II) departure, would give the final product **15**.

The aforementioned structures are depicted in Figure 7a, and the corresponding energies are reported in Table 8 and drawn in Figure 7b. The pathway through **18** is preferred, according to the B3LYP results. As for the HF/3-21G calculations, although the profiles obtained are slightly different, this trend is maintained. In any case, at the two theoretical levels the highest point in the energy

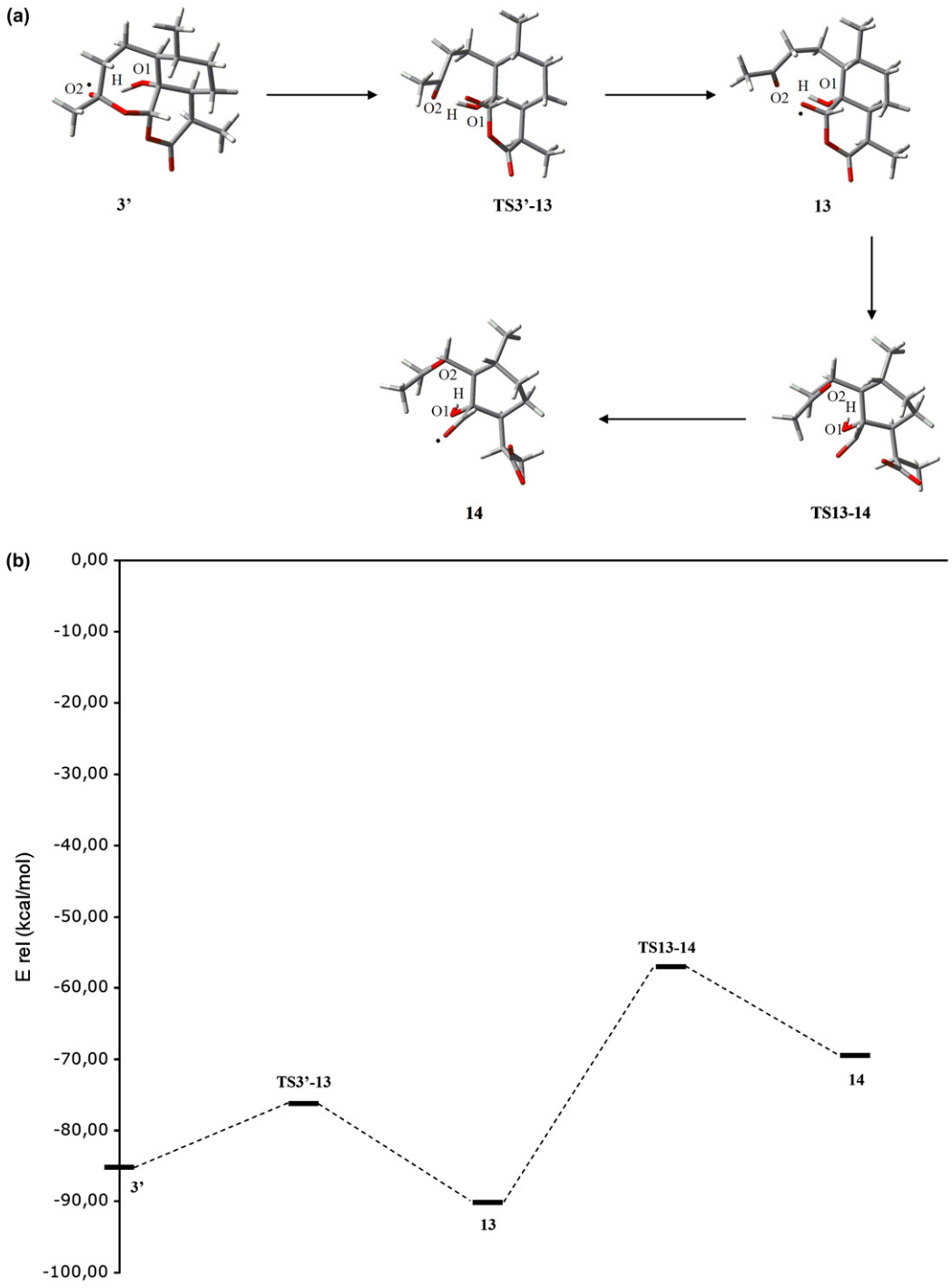

Figure 6. (a) Stationary points **3′**, **13**, **14**, **TS3′–13**, and **TS13–14**. (b) Energy profiles for the steps leading from **3′** to **14** at B3LYP level.

profiles is found to be **TS17–15**, and hence if **15** is to be reached, the two pathways could compete if a connection do exists between **13** and **16**.

The results in Table 1 show that at **16** the unpaired electron is found at O1, as expected, and at **17** the spin density is found at C8. Transition state **TS16–17** shows an early character, because the unpaired electron is mainly localized at O1, with a lower value of the spin density on C8. At **TS17–15**, the unpaired electron moves to H_{O9} that will be released as a hydrogen atom in our model system.

The second pathway from **13** begins with **TS13–18**, in which the unpaired electron is partitioned between O9 and, to a lesser extent, C7. At **18**, the spin density is found at C7, as expected, and **TS18–17** shows a delocalization of the unpaired electron between C7 and C8, with no remarkable spin density found on O9, O1, or the H being transferred.

Table 7
Energy values (E, hartree/particle) for the indicated stationary points obtained at B3LYP level. Relative energies (E_{rel}, kcal/mol) to **1** plus an H atom

	E	E_{rel}
3′	−961.544363	−85.26
TS3′–13	−961.530088	−76.30
13	−961.552274	−90.23
TS13–14	−961.499512	−57.12
14	−961.519356	−69.57

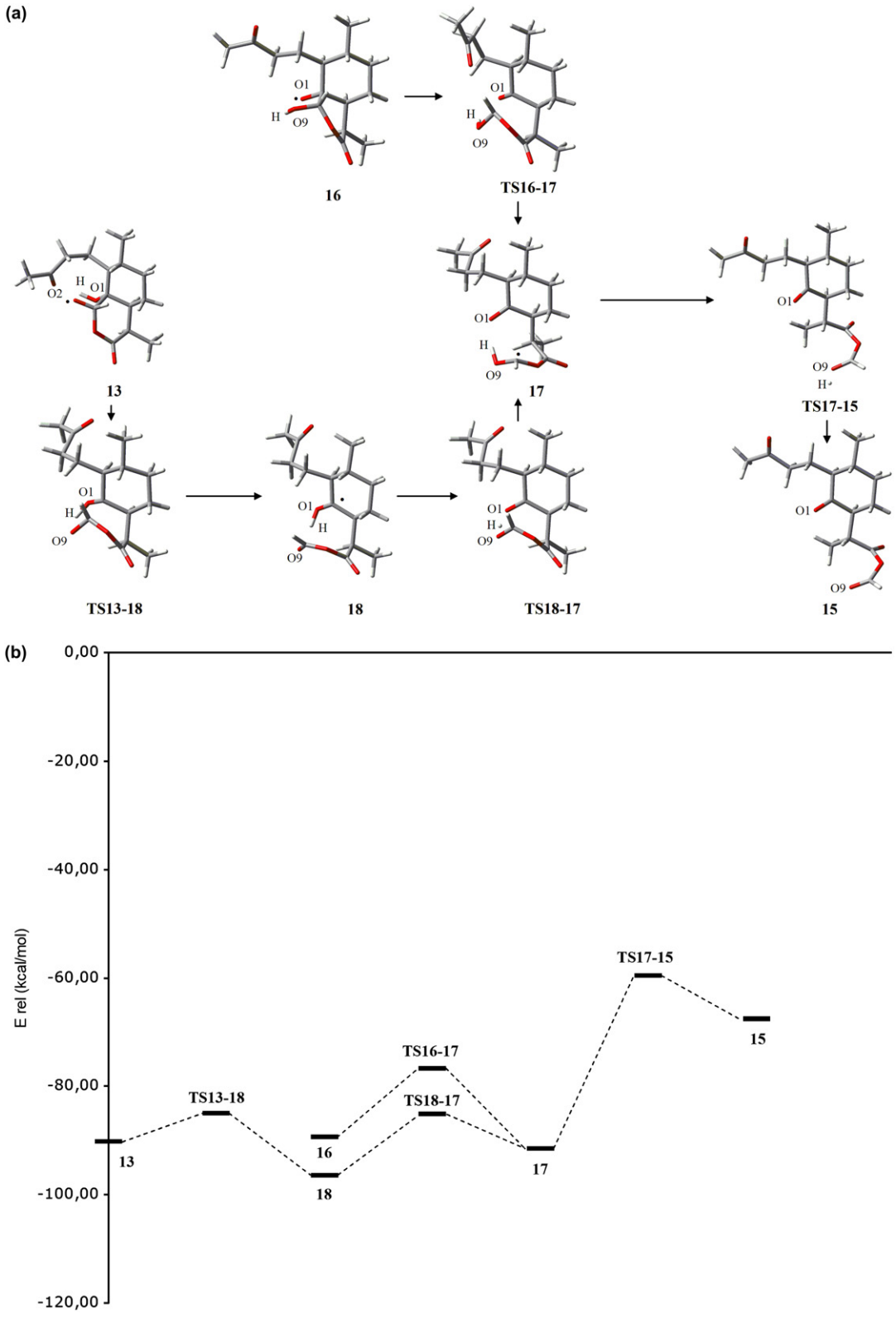

Figure 7. (a) Stationary points **13**, **16**, **17**, **18**, **15**, **TS16–17**, **TS17–15**, **TS13–18**, and **TS18–17**. (b) Energy profiles for the steps leading from **13** to **15** at B3LYP level.

3.8. The whole set of mechanisms

To obtain a global view of the processes studied, it is very convenient to assemble the fragments. In Figure 8a, the energy profile for the O1 radical route is drawn. Starting from **1**, the pathways obtained by using the B3LYP/6-31G(d,p) theoretical level up to the products **6** and **8** are presented. This view reveals that the two final products are very close in energy to each other, being **8** more stable than **6**, the energetic difference being ca. 8 kcal/mol. The same can be said about the transition structures of maximum energy in the

Table 8
Energy values (E, hartree/particle) for the indicated stationary points obtained at B3LYP level. Relative energies (E_{rel}, kcal/mol) to **1** plus an H atom

	E	E_{rel}
13	−961.552274	−90.23
TS13–18	−961.543958	−85.01
18	−961.562372	−96.56
TS18–17	−961.544289	−85.21
17	−961.554388	−91.55
TS17–15	−961.503644	−59.71
15+H	−961.516142	−67.55
16	−961.550929	−89.38
TS16–17	−961.530890	−76.81

pathways of minimum energy connecting the carbon-centered radicals **4** to each one of the products, cf. **TS5**–**6** and **TS7**–**8** for the routes to **6** and **8**, respectively. It is also interesting to note that all points in the reported routes lie under the energy value of the initial **TS1**–**2**, thus assuring the products' formation if the reaction is initiated. The competition between the paths yielding **6** and **8** will be resolved mainly as a function of the experimental conditions, thus explaining the different yields observed in the different experimental studies of artemisinin decomposition. We have not included in Figure 8a, the path from **4**″ plus a hydrogen atom to **8** plus a water molecule: as stated before, such a path would be preferred only in the case that a hydrogen atom source was found in the medium.

In Figure 8b, the energy profile for the O2 radical route is drawn. In this case, starting from **1**, the pathways yielding the final products **12** and **15** are reported. It must be said that **14** is not a final product, but a radical that would further evolve to other species not studied here, see Scheme 2. It is revealed again that the two products are very close in energy to each other, being **15** more stable than **12** by only ca. 1 kcal/mol. In this case, however, there is a slightly larger difference between the energies of the transition structures of maximum energy in the pathways of minimum energy connecting the reactants to each one of the products, cf.

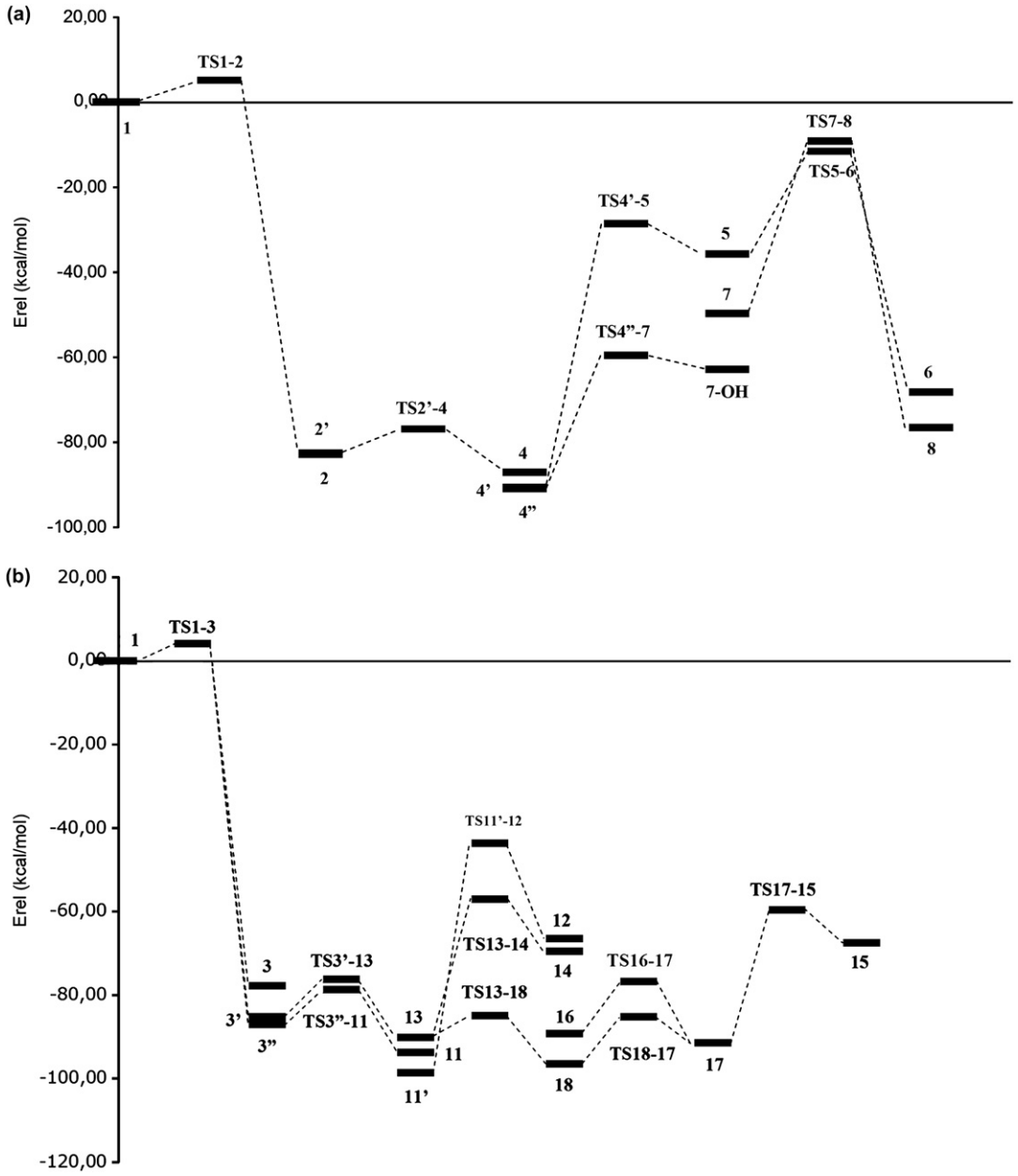

Figure 8. (a) Energy profiles for the O1 radical route, calculated at B3LYP/6-31 G(d,p) level. (b) Energy profiles for the O2 radical route, calculated at B3LYP/6-31 G(d,p) level.

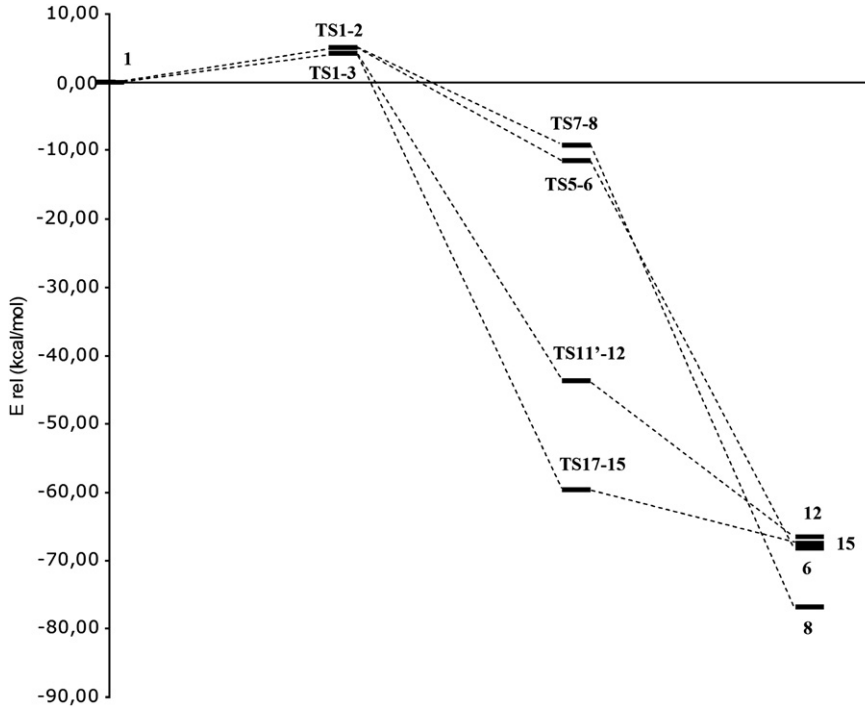

Figure 9. Comparative energies of the reactants, the initial TSs, the TSs of highest energy found along the minimum energy pathways studied, and the species modeling the experimentally obtained products, as calculated by means of B3LYP/6-31G(d,p) theoretical level.

TS11′–12 and **TS17–15** for the routes to **12** and **15**, respectively. All points in the reported routes lie again under the energy value of the initial **TS1–3**, and the products formation and the competition between the paths would take place as before. These results fairly reproduce our previously obtained conclusions.[48]

The aforementioned observations are even clearer in Figure 9, in which only the starting reactants, the initial TSs, the TSs of maximum energy along the minimum energy O1 and O2 radical routes, and the final products are sketched. From this figure it can be seen that the products **12** and **15** are predicted to be formed in an easier way, and that the formation of **8** and **6** is also straightforward once the reaction is initiated, because the highest point to surmount is the initial TS for all cases. It can also be appreciated that the four final products lie very close in energy to each other, being **8** the more stable one and **12** the less stable one, and the energetic difference between them being of only ca. 10 kcal/mol. According to the results herein reported, if the solvent used is not very polar, and therefore has a passive role, it is expected to obtain **8** as the major product, as it is indeed found.[52] In this sense, our calculations nicely explain the experimental results.

4. Conclusions

The results reported in the present work explain the appearance of the final products in a satisfactory way. The intermediates and radicals have been found as relatively stable species, thus giving support to the current hypothesis that some of such species can be responsible for the antimalarial action of artemisinin and its derivatives, either by hitting specific targets within the parasite or by disrupting the hemozoin polymerization process and causing in this way the *plasmodium* death. Some specific conclusions can also be derived from this work:

(a) The products' formation is assured once the reaction is initiated, and the different paths will compete depending on the experimental conditions.

(b) We have confirmed that a TS do exist modeling the interconversion between the initial *O*-centered radicals, showing that the O1 and O2 radical routes are intimately related.

(c) A possible second link between the two radical routes has been found, via **TS3″–4″**. If this transition structure did exist in the actual system, new pathways rarely proposed in the literature would be opened, giving rise to products other than the ones usually characterized. To establish the relevance of this finding, or discarding it as an artifact of the molecular model used, further experimental and theoretical works are needed.

(d) In agreement with recent work[45] and with our previous paper,[48] it is concluded that the epoxide intermediate is probably not responsible of the antimalarial activity, because other intermediates are found to be more stable and potentially more active as alkylating agents.

(e) The obtaining of **15** involves three different steps from the oxygen-centered radical **13**, instead of a single step as it was originally suggested.

(f) From the C4 secondary radical **4**, the outcome of **8**, one of the experimentally detected products in the artemisinin decomposition, can take place through the alkene intermediate **7** or via the intermolecular H abstraction from the medium to form the intermediate **9**. If there is a source of H, the second path is found to be preferable and the existence of two alternative mechanisms assures that **8** will be reached, as it is observed experimentally. The formation of **8** from **9** is carried out by means of a concerted step; it does not take place through a two-step mechanism as it was postulated.

(g) One of the stationary points (**TS13–16**) was found at HF/3-21G level, but not by using the B3LYP/6-31G(d,p) calculations. This fact could suggests that actually only one of the paths herein studied connecting **13** with **18** takes place.

(h) The C4 primary radical **11** is found to be the most stable structure within the initial steps of the artemisinin decomposition and hence the O2 radical route is calculated to be thermodynamically favored until the *C*-radicals are formed.

This agrees with the in vivo experiments in that the only fully characterized alkylation reaction reported to date in infected mice is the heme alkylation by means of the C4 primary radical.[15,24]

The work herein reported was conducted with the aim of reinforcing, or changing if this was the case, the conclusions reached in our previous paper.[48] In that report, we used a relatively simple molecular model and doubts could be raised upon the accuracy of the model, because the rings close to the trioxane moiety were not included. As can be seen in the present work, we have essentially reproduced the same mechanistic steps obtained in the previous study, and either from a qualitative or from a quantitative point of view the conclusions reached remains unchanged. These are good news when facing further studies demanding harder computing power: the inclusion in the molecular model of the Fe(II) ion that initiates the cascade of reactions from the artemisinin to the final products can be done with confidence by using the simplest model. Also, the inclusion of the solvent effects that can be determinant in discriminating between the possible pathways can take benefit from using the small model. The way by which the potentially antimalarial intermediates hit the putative targets can also be studied with the simple model previously used. Our group is conducting these studies and the results obtained will hopefully be reported in due form, with the ultimate aim of contributing to a better understanding of the antimalarial activity of artemisinin and its derivatives.

Acknowledgements

Financial support by the Generalitat Valenciana (Project GV04B-029) and Fundació Bancaixa-UJI (P1 1B2005-15 and P1 1B2005-27) is gratefully acknowledged. P.M. acknowledges the Generalitat Valenciana for the grant TS/05/UJI/02 and the Universitat Jaume I for the grant PREDOC/2005/28.

Supplementary data

Tables containing total and relative energy values (at HF/3-21G level) for the stationary points leading: from **1** to **2′** and **3′** (Table 1S); from **2′** to **4″** and from **3″** to **11**, as well as **TS3″–4″** (Table 4S); from **4′** to **6** (Table 7S); from **4″** to **8** (Table 10S); from **11′** to **12** (Table 13S); from **3′** to **14** (Table 16S); from **13** to **15** (Table 19S).

Tables containing imaginary frequencies, unique negative eigenvalues, and main components of the transition vectors and the corresponding geometric parameters for the following TSs, obtained at B3LYP/6-31G(d,p) and HF/3-21G levels: **TS1–2**, **TS1–3**, and **TS2′–3′** (Tables 2S and 3S); **TS2′–4**; **TS3″–11** and **TS3″–4″** (Tables 5S and 6S); **TS4′–5** and **TS5–6** (Tables 8S and 9S); **TS4″–7**, **TS7–8**, **TS9–8a** and **TS9–8b** (Tables 11S and 12S); **TS11′–12** (Tables 14S and15S); **TS3′–13** and **TS13–14** (Tables 17S and 18S); **TS13–18**, **TS18–17**, **TS17–15**, **TS13–16** (only at HF/3-21G level) and **TS16–17** (Tables 20S and 21S).

This material is available free of charge via Internet. Supplementary data associated with this article can be found in the online version, at doi:10.1016/j.tet.2008.07.086.

References and notes

1. Haynes, R. K.; Ho, W.-Y.; Chan, H.-W.; Fugmann, B.; Stetter, J.; Croft, S. L.; Vivas, L.; Peters, W.; Robinson, B. L. *Angew. Chem., Int. Ed.* **2004**, *43*, 1381–1385.
2. Drew, M. G. B.; Metcalfe, J.; Dascombe, M. J.; Ismail, F. M. D. *J. Med. Chem.* **2006**, *49*, 6065–6073.
3. McMichael, A. J.; Woodruff, R. E.; Hales, S. *Lancet* **2006**, *367*, 859–869.
4. Tonmunphean, S.; Parasuk, V.; Kokpol, S. *Bioorg. Med. Chem.* **2006**, *14*, 2082–2088.
5. O'Neill, P. M.; Posner, G. H. *J. Med. Chem.* **2004**, *47*, 2945–2964.
6. Posner, G. H.; O'Neill, P. M. *Acc. Chem. Res.* **2004**, *37*, 397–404.
7. Meshnick, S. R.; Taylor, T. E.; Kamchonwongpaisan, S. *Microbiol. Rev.* **1996**, *60*, 301–315.
8. Pinheiro, J. C.; Kiralj, R.; Ferreira, M. C. *QSAR Comb. Sci.* **2003**, *22*, 830–842.
9. Krishna, S.; Woodrow, C.; Staines, H. M.; Haynes, R. K.; Mercerau-Puijalon, O. *Trends Mol. Med.* **2006**, *12*, 200–205.
10. White, N. J. *J. Clin. Invest.* **2004**, *113*, 1084–1092.
11. Gu, J.; Chen, K.; Jiang, H.; Leszczynski, J. *J. Phys. Chem. A* **1999**, *103*, 9364–9369.
12. Taranto, A. G.; Carneiro, J. W. d. M.; de Oliveira, F. G.; de Araujo, M. T.; Correa, C. R. *J. Mol. Struct. (THEOCHEM)* **2002**, *580*, 207–215.
13. Robert, A.; Dechy-Cabaret, O.; Cazelles, J.; Meunier, B. *Acc. Chem. Res.* **2002**, *35*, 167–174.
14. Robert, A.; Benoit-Vical, F.; Claparols, C.; Meunier, B. *Proc. Natl. Acad. Sci. U.S.A.* **2005**, *102*, 13676–13680.
15. Tang, Y.; Dong, Y.; Wang, X.; Sriraghavan, K.; Wood, J. K.; Vennerstrom, J. L. *J. Org. Chem.* **2005**, *70*, 5103–5110.
16. Messori, L.; Gabbiani, C.; Casini, A.; Siragusa, M.; Vincieri, F. F.; Bilia, A. R. *Bioorg. Med. Chem.* **2006**, *14*, 2972–2977.
17. Golenser, J.; Waknine, J. H.; Krugliak, M.; Hunt, N. H.; Grau, G. E. *Int. J. Parasitol.* **2006**, *36*, 1427–1441.
18. Meshnick, S. R.; Thomas, A.; Ranz, A.; Xu, C. M.; Pan, H. Z. *Mol. Biochem. Parasitol.* **1991**, *49*, 181–190.
19. Posner, G. H.; Oh, C. H. *J. Am. Chem. Soc.* **1992**, *114*, 8328–8329.
20. Wu, Y. *Acc. Chem. Res.* **2002**, *35*, 255–259.
21. Butler, A. R.; Gilbert, B. C.; Hulme, P.; Irvine, L. R.; Renton, L.; Whitwood, A. C. *Free Radic. Res.* **1998**, *28*, 471–476.
22. Wu, W.-M.; Wu, Y.; Wu, Y.-L.; Yao, Z.-J.; Zhou, C.-M.; Li, Y.; Shan, F. *J. Am. Chem. Soc.* **1998**, *120*, 3316–3325.
23. O'Neill, P. M.; Bishop, L. P.; Searle, N. L.; Maggs, J. L.; Ward, S. A.; Park, B. K.; Mabbs, F. *J. Org. Chem.* **2000**, *65*, 1578–1582.
24. Robert, A.; Bonduelle, C.; Laurent, S. A.-L.; Meunier, B. *J. Phys. Org. Chem.* **2006**, *19*, 562–569.
25. Kannan, R.; Kumar, K.; Sahal, D.; Kukreti, S.; Chauhan, V. S. *Biochem. J.* **2005**, *385*, 409–418.
26. Zhang, F.; Gosser, D. K.; Meshnick, S. R. *Biochem. Pharmacol.* **1992**, *43*, 1805–1809.
27. Robert, A.; Meunier, B. *Chem. Soc. Rev.* **1998**, *27*, 273–279.
28. Robert, A.; Cazelles, J.; Meunier, B. *Angew. Chem., Int. Ed.* **2001**, *40*, 1954–1957.
29. Cazelles, J.; Robert, A.; Meunier, B. *J. Org. Chem.* **2002**, *67*, 609–619.
30. Olliaro, P.; Haynes, R. K.; Meunier, B.; Yongyuth, Y. *Trends Parasitol.* **2001**, *17*, 123–126.
31. Eckstein-Ludwig, U.; Webb, R. J.; van Goethem, I. D. A.; East, J. M.; Lee, A. G.; Kimura, M.; O'Neill, P. M.; Bray, P. G.; Ward, S. A.; Krishna, S. *Nature* **2003**, *424*, 957–961.
32. Ridley, R. G. *Nature* **2003**, *424*, 887–889.
33. Haynes, R. K.; Monti, D.; Taramelli, D.; Basilico, N.; Parapini, S.; Olliaro, P. *Antimicrob. Agents Chemother.* **2003**, *47*, 1175.
34. Yang, Y. Z.; Asawamahasakda, W.; Meshnick, S. R. *Biochem. Pharmacol.* **1993**, *46*, 336–339.
35. Yang, Y. Z.; Little, B.; Meshnick, S. R. *Biochem. Pharmacol.* **1994**, *48*, 569–573.
36. Asawamahasakda, W.; Ittarat, I.; Pu, Y. M.; Ziffer, H.; Meshnick, S. R. *Antimicrob. Agents Chemother.* **1994**, *38*, 1854–1858.
37. Bhisutthibhan, J.; Philbert, M. A.; Fujioka, H.; Aikawa, M.; Meshnick, S. R. *Eur. J. Cell Biol.* **1994**, *78*, 665–670.
38. Pandey, A. V.; Tekwani, B. L.; Singh, R. L.; Chauhan, V. S. *J. Biol. Chem.* **1999**, *274*, 19383–19388.
39. Bhisutthibhan, J.; Meshnick, S. R. *Antimicrob. Agents Chemother.* **2001**, *45*, 2397–2399.
40. Cumming, J. N.; Ploypradith, P.; Posner, G. H. *Adv. Pharmacol.* **1996**, *37*, 253–297.
41. Drew, M. G. B.; Metcalfe, J.; Ismail, F. M. D. *J. Mol. Struct. (THEOCHEM)* **2004**, *711*, 95–105.
42. Tonmunphean, S.; Parasuk, V.; Kokpol, S. *J. Mol. Struct. (THEOCHEM)* **2005**, *724*, 99–105.
43. Wiwanitkit, V. *J. Infect.* **2006**, *53*, 148–151.
44. Arantes, C.; de Araujo, M. J.; Taranto, A. G.; de Carneiro, J. W. *Int. J. Quantum Chem.* **2005**, *103*, 749–762.
45. Taranto, A. G.; Carneiro, J. W. d. M.; de Araujo, M. T. *Bioorg. Med. Chem.* **2006**, *14*, 1546–1557.
46. de Araujo, M. J.; de Carneiro, J. W.; Taranto, A. G. *Int. J. Quant. Chem.* **2006**, *106*, 2804–2810.
47. Drew, M. G. B.; Metcalfe, J.; Ismail, F. M. D. *J. Mol. Struct. (THEOCHEM)* **2005**, *756*, 87–95.
48. Moles, P.; Oliva, M.; Safont, V. S. *J. Phys. Chem. A* **2006**, *110*, 7144–7158.
49. McIver, J. W., Jr. *Acc. Chem. Res.* **1974**, *7*, 72–77.
50. Fukui, K. *J. Phys. Chem.* **1970**, *74*, 4161–4163.
51. Frisch, M. J.; Trucks, G. W.; Schlegel, H. B.; Scuseria, G. E.; Robb, M. A.; Cheeseman, J. R.; Zakrzewski, V. G.; Montgomery, J. A., Jr.; Stratmann, R. E.; Burant, J. C.; Dapprich, S.; Millam, J. M.; Daniels, A. D.; Kudin, K. N.; Strain, M. C.; Farkas, O.; Tomasi, J.; Barone, V.; Cossi, M.; Cammi, R.; Mennucci, B.; Pomelli, C.; Adamo, C.; Clifford, S.; Ochterski, J.; Petersson, G. A.; Ayala, P. Y.; Cui, Q.; Morokuma, K.; Malick, D. K.; Rabuck, A. D.; Raghavachari, K.; Foresman, J. B.; Cioslowski, J.; Ortiz, J. V.; Baboul, A. G.; Stefanov, B. B.; Liu, G.; Liashenko, A.; Piskorz, P.; Komaromi, I.; Gomperts, R.; Martin, R. L.; Fox, D. J.; Keith, T.;

Al-Laham, M. A.; Peng, C. Y.; Nanayakkara, A.; Gonzalez, C.; Challacombe, M.; Gill, P. M. W.; Johnson, B.; Chen, W.; Wong, M. W.; Andres, J. L.; Gonzalez, C.; Head-Gordon, M.; Replogle, E. S.; Pople, J. A. *Gaussian 98*; Gaussian: Pittsburgh, PA, 1998.

52. Posner, G. H.; Cumming, J. N.; Ploypradith, P.; Oh, C. H. *J. Am. Chem. Soc.* **1995**, *117*, 5885–5886.
53. Pereira, M. S. C.; Kiralj, R.; Ferreira, M. M. C. *J. Chem. Inf. Model.* **2008**, *48*, 85–98.
54. Harvey, J. N.; Ascgi, M.; Schwarz, H.; Koch, W. *Theor. Chem. Acc.* **1998**, *99*, 95–99.
55. Avery, M. A.; Fan, P.-C.; Karle, J. M.; Bonk, J. D.; Miller, R.; Goins, D. K. *J. Med. Chem.* **1996**, *39*, 1885–1897.